ECAP-2018

Surface survey of an aspherical mirror for the CTA-observatory

Bachelorarbeit aus der Physik

Vorgelegt von
Johann Brand
27.07.2018

Erlangen Centre for Astroparticle Physics
Physikalisches Institut I
Friedrich-Alexander-Universität Erlangen-Nürnberg

1. Betreuer: Prof. Dr. Christopher van Eldik
2. Betreuer: Prof. Dr. Stefan Funk

Abstract

Since humankind's interest in observing the night sky has been awakened, appropriate research methods have also been promoted. In the year 1912, Viktor F. Hess was the first to discover cosmic rays. Through his scientific discovery, several new observation methods could be used. The next step in this research evolution is the so-called CTA, which is an abbreviation for the Cherenkov Telescope Array. It will cover an area of roughly $4km^2$ and it will be capable to measure Energies of a few tens GeV to about 300TeV. Therefore, several designs of telescopes are planned. One of them is the mid-size Schwarzschild-Couder telescope (SCT), consisting out of two mirrors, to receive advantages such as a wider view of few. SCTs bring not only spherical, but also aspherical mirrors with them. A procedure has already been developed to analyse the quality of the mirrors.
The goals of this thesis were, first to improve measurement qualities for small spherical mirrors and second to verify measuring accuracy for a strongly curved aspherical mirror. Moreover, due to the calibration of the short-working-distance-3 (SWD-3), a comparison to the older short-working-distance-2 (SWD-2) measuring setup was made.

Contents

1 Introduction to high energy gamma ray astronomy **3**
1.1 Sources of gamma rays . . . 3
1.2 Cherenkov radiation and high-energy gamma rays . . . 4
1.3 CTA-telescopes . . . 5

2 Schwarzschild-Couder telescope **7**
2.1 Schwarzschild-Couder design . . . 7
2.2 Segmentation . . . 7
2.3 Mirror description . . . 9

3 Phase measuring deflectometry **11**
3.1 Measuring setup . . . 11
3.2 Pixel mapping . . . 11
3.3 Optimisation of mirror position . . . 12
3.4 Point spread function . . . 13
3.5 Point spread of an aspherical mirror . . . 13

4 Measurement of small size mirror **15**

5 Measuring aspherical mirror P2 facets **19**
5.1 Measuring simulated aspherical mirror . . . 19
5.2 Measuring real aspherical P2.029 mirror . . . 22
5.3 Comparison and discussion . . . 24

6 Comparison of SWD-2 and SWD-3 **25**
6.1 Measurement of sanko mirror with SWD-2 . . . 25
6.2 Measurement of sanko mirror with SWD-3 . . . 26
6.3 Comparison and discussion . . . 30

7 Summary and outlook **31**

8 Appendix **32**

Acknowledgements **35**

Statement of Authorship **36**

1 Introduction to high energy gamma ray astronomy

Hess's discovery of cosmic rays in the year 1912 opened the door to many new discoveries in particle and astroparticle physics (see Blümer et al. 2009). In addition to that, the famous balloon flights brought him the Nobel prize in the year 1936. Sources of this charged particles are called cosmic accelerators. Pions, positrons and muons where the first discovered, which later called part of the secondary cosmic rays, which are produced through the decay of primary cosmic radiation such as Protons or Alpha-particles (99%). Astroparticle physics deals with charged particles for learning something about the sources of these rays. However, this brings a problem, because these particles are electrically charged and can be deflected by cosmic magnetic fields while travelling through the universe to earth. So the information about the source candidates is limited. Remedy brings a so-called By-product of these sources, the gamma rays, which compared to charged particles travel in straight lines. This characteristic is used to identify the source point.
Since 1936, there are many new ways to investigate cosmic rays. On the one hand, space based telescopes, e.g. FERMI-LAT, are used, surrounding the earth, measuring γ-rays by e^-e^+ pair production. On the other hand, ground based telescopes are utilized to detect gamma rays via the detection of Cherencov light emitted by the gamma rays when they travel through the atmosphere of the earth. One advantage of such ground based telescopes such as H.E.S.S. or CTA, which is in planning, is their higher sensitivity for low flux, high-energy gamma rays, because of their huge detector area.

1.1 Sources of gamma rays

Presumable sources for high energy cosmic rays and also gamma rays are Supernova remnants (SNR), surrounding nebular of pulsars, active galactic nuclei (AGN) and gamma ray bursts (GRB's) (see Tinivella 2016). Dark matter annihilation is supposed to be a gamma ray sources as well. Supernova remnants considered the major source of galactic cosmic rays. Accelerated particles in SNRs are principally protons, He nuclei and e^- from the shocked matter. However, collisions between high energy particles and the SNR matter can result in the production of secondary particles like $p\overline{p}$ and e^-e^+ pairs. The so produced antiparticles are accelerated in the same way of ordinary particles (see Blasi 2009). Now pair annihilation, synchrotron radiation and inverse Compton scattering produce the high-energy gamma rays. An alternative way is that high-energy protons produce photons via π^0 production. The result is a 68MeV[1] peak in gamma ray spectrum. This ways of producing gamma rays is called the hardronic and leptonic channel. While acceleration in SNR takes place through a shock wave, in surrounding nebular of pulsars this occurs by rotating magnetic fields of the pulsar.

[1] half of the π^0 mass

1.2 Cherenkov radiation and high-energy gamma rays

If a particle has a velocity v which is higher than the speed of light in the medium it is travelling in, it emits Cherenkov radiation. The light emits in a cone with an aperture angle depending on the velocity of the particle and the refrective index of the surrounding media, following equation 1.

$$cos\,(\theta) = \frac{c_{medium}}{v_{particle}} = \frac{1}{n\beta} \tag{1}$$

This phenomenon finds usage in the detection of high energy γ-rays, shown in

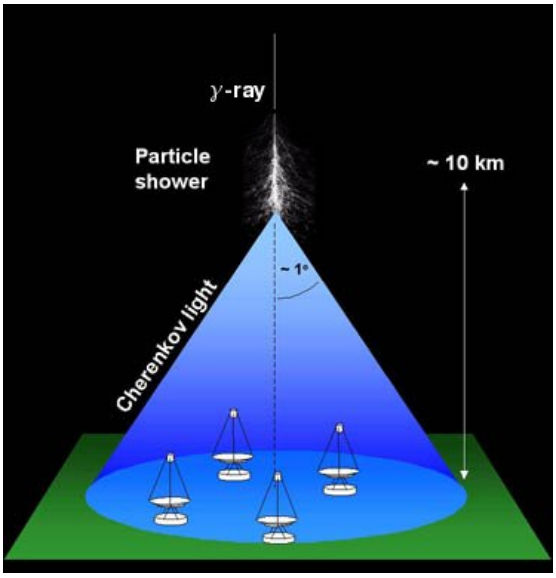

Figure 1.1: A γ-ray interacts in the atmosphere and produces secondary particles in an air shower. Those move faster than the speed of light in air and so emit Cherenkov light in form of a cone. Interaction starts in about 10km above earth. The cones aperture angle is usualy $\sim 1°$ (Image from Durham University 2014).

Figure 1.2. When they interact in the upper part of the atmosphere, there will be secondary particles produced. They on their own emit photons by Bremsstrahlung and secondary particles so that an electro magnetic cascade appeares. These air showers will be detected in form of Cherenkov light with systems like H.E.S.S, see figure 1.1. The discribed secondary particles are mostly electrons and positrons, which have a greater velocity than the speed of light in the surrounding medium. An important feature for showers produced by gamma rays, is that there are no muons, pions and other debris produced (for more information see Longair 1992). For γ-rays the first interaction in the atmosphere is at around 10km above see level. The aperture is about $1°$ and the size of the pool of Cherenkov light is typically about $10^4 m^2$. The weak blueish light[2] flashes require a huge light

[2]its density is inversely related to the wavelength squared. Therefore, the number of photons increases as the wavelength decreases. That explains why most of the Cherenkov radiation seems blue and mostly in UV range.(for more information see Stanford University 2014)

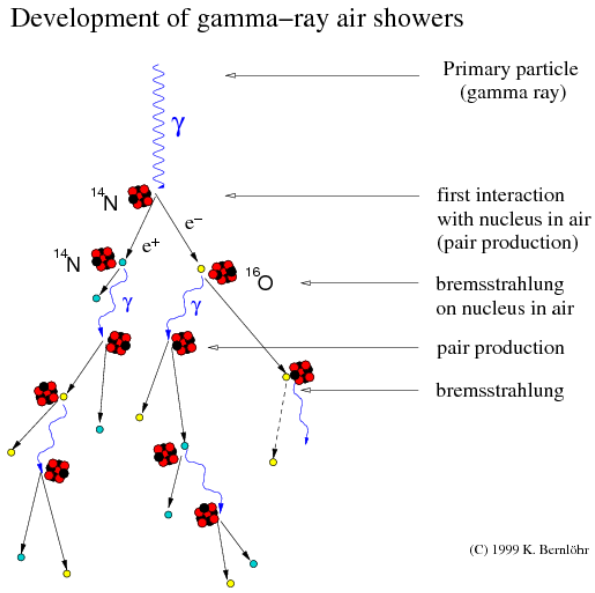

Figure 1.2: Schematic of air shower development. A primary particle, in this case a gamma ray interacts in presence of a nucleus, through pair production in an electron positron pair. They on their own produce again a γ-ray via Bremsstrahlung. These processes take part again and again and summed up build a shower event. (Image from Cui 2009)

detection surface, dark nights and a very short exposure time of the cameras[3] (see Durham University 2014).

1.3 CTA-telescopes

The Cherenkov-Telescope-Aray, short CTA, is the next step in evolution of high-energy gamma-ray astronomy. It will be an observatory on two sites on Earth (see Consortium 2018). One array will most likely be located at the European Southern Observatory (ESO) Paranal grounds in Chile (CTA-south) and the other at Instituto de Astrofisica de Canarias (IAC), Roque de los Muchachos Observatory in La Palma, Spain (CTA-north). The southern site is less than 10 km south-east of ESO's existing Paranal Observatory in the Atacama Desert, which is considered one of the driest and most isolated regions on earth and therefore ideal for astronomical observatories. Each array consists of several telescopes in three different sizes. All in all, on both locations together over one hundred telescopes are planned, aiming to provide energy coverage for gamma rays from 20GeV to at least 300TeV, to give CTA reach to high-redshift and extreme accelerators (see Acharya et al. 2018). Furthermore a substantially improvement of the angular resolution and of the field of view is sought, in order to enable imaging extended sources and even more. The broad energy range, CTA will be able to measure, comes from the usage of three different sized telescopes. The large size telescopes (LST) with a field of view of 4.5°, an energy coverage of $E < 100GeV$ and a

[3]for H.E.S.S. exposure time is $16ns$ (see Balzer 2012)

diameter of 24m. Second, the medium size telescope (MST) with a diameter of 12m, an energy range of 0.1-10TeV and a 6° large field of view. Thirdly, with a diameter of 6m, the small size telescope (SST), providing an energy range above 10TeV and a field of view of about 8°. The amount of telescopes increases with decreasing diameter so that about 70 of 100 telescopes are SST's. The array in the North will consist of 4 LSTs and 15 MST's. 4 LSTs, 25 MSTs and additional 70 SSTs will perform measurements on the southern hemisphere (Consortium 2018). Finally there are not only differences in sizes and layouts assembling the telescopes, but also in designs planned. One of them is the Davies-Cotton (DC) design, consisting of spherical mirrors, which is also used at H.E.S.S.. This design is the only one planned to use for LST's. It finds its usage in MST's and SST's as well. For the two smaller ones, there is an alternative design, especially invented for CTA, planned. The Schwarzschild-Couder telescopes (SC), which brings up a wider field of view with less aberrations. In figure 1.3, the two medium size telescope layouts are shown.

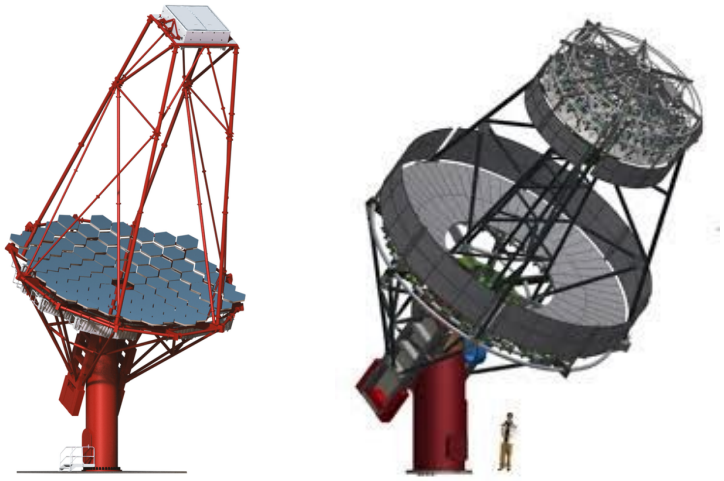

(a) Davies-Cotton telescope layout

(b) Schwarzschild-Coulder telescope layout

Figure 1.3: Left: Illustration of a 12m diameter Davis-Cotton telescope (Image from CTA-Colaboration 2017). On the right: CAD model of the full size prototype Schwarzschild-Couder telescope (pSCT) under construction at the Fred Lawrence Whipple Observatory in Arizona (Image from Rousselle et al. 2015).

2 Schwarzschild-Couder telescope

In this chapter the Schwarzschild-Couder telescope and its mirrors are described because information about mirror design is needed for further evaluation. Focus of description is on MST's, since the aspherical mirror which is tested elsewhere in this thesis belongs to this certain kind of telescope.
At Erlangen center for astroparticle physics (ECAP), a aspherical mirror has already been evaluated by (see Specovius 2016). Now a second facet of the prototype MST Schwarzschild-Coulder telescope is available. In the following subsections, the focus is on the design of the telescope and its unique mirror segmentation.

2.1 Schwarzschild-Couder design

The Schwarzschild-Couder medium-sized telescope (SC-MST) is a candidate telescope for CTA, which utilizes a novel two mirrors optical design with an aperture of 9.5 m, see figure 2.1. This design offers a wide field of view of 8 degrees, improves the angular resolution compared to current single mirror imaging atmospheric cherenkov telescopes (IACTs) and reduces the plate scale of the camera enabling the use of novel SiPM(silicon photomultiplier) photosensors (see Rousselle et al. 2015). Second advantage of smaller plate scales is a cost reduction by being able to use smaller cameras. However, the design is characterised by three distances. The distance between the two mirrors

$$\frac{F}{q}, \tag{2}$$

depending on the focal length F and a variable q, that between the second mirror and the focal plane

$$(1-a)F, \tag{3}$$

depending on the focal length F and a variable a and thirdly on the focal length

$$F, \tag{4}$$

see figure 2.2. Performance estimations brought up the values $a = \frac{2}{3}$ for and $q = \frac{2}{3}$ (for more information see Vassiliev & Rousselle 2012).

2.2 Segmentation

Both primary (4.83 m radius) and secondary (2.71 m radius) mirror are too large to be inexpensively produced as one single mirror and have to be segmented for cost reduction. While the primary mirror P is segmented in two panels with 16 and 32 elements, the secondary, S consists of 8 and 16 elements (see Rousselle et al. 2015). The arrangement of them is shown in figure 2.3. Due to rotational symmetry, each segment of the same ring, equals to each other. To distinguish between the outer and inner mirrors, they received an index 1 for the inner and 2 for the outer ring. In table 2.1 the most important values of segmentation are summarised.

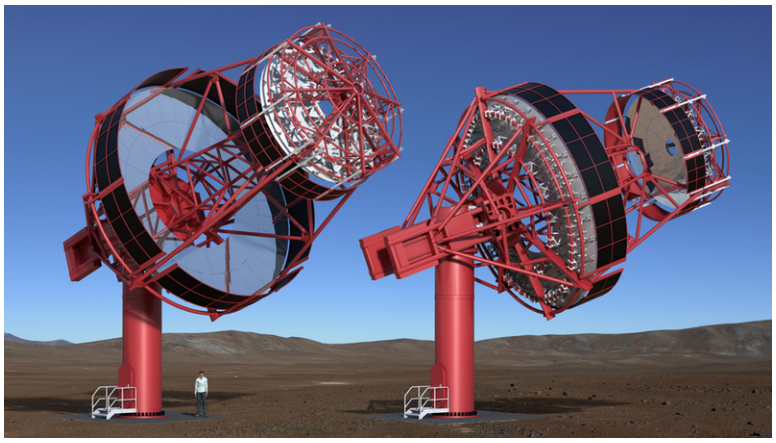

Figure 2.1: Above, a Schwarzschild-Couder Telescope mechanical design of the prototype in Arizona (Image from CTA-Colaboration 2018).

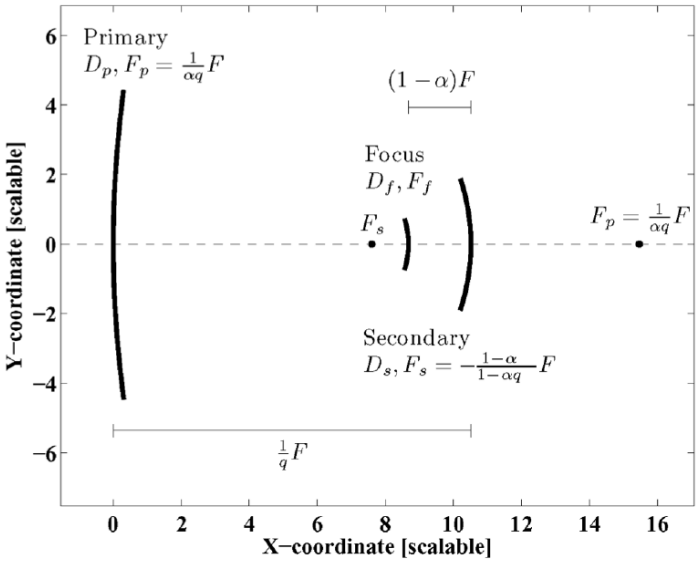

Figure 2.2: The geometrical configuration of the Schwarzschild-Couder telescope is defined by its focal length, F, and by two other parameters a and q, which determine the focal plane of the system and the position of the primary and secondary mirror (Image from Vassiliev & Rousselle 2012).

Mirror panel	P1	P2	S1	S2
Number of panels	16	32	8	16
Radius max $[m]$	3.4	4.83	1.60	2.71
Radius min $[m]$	2.19	3.40	0.39	1.60
Diagonal $[m]$	1.61	1.64	1.35	1.38
Panel area $[m^2]$	1.33	1.16	0.94	0.94

Table 2.1: Definition of the mirror panels. P1 and P2 are respectively the inner and outer mirror panels of the primary mirror, while S1 and S2 correspond to the inner and outer mirror panels of the secondary mirror (for more information see Vassiliev & Rousselle 2013)

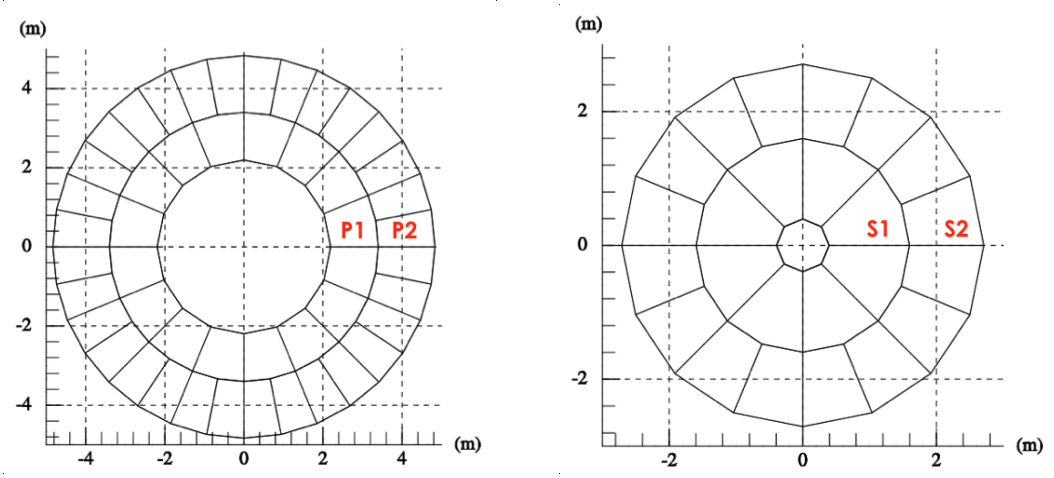

(a) Davies-Cotton telescope layout (b) Schwarzschild-Coulder telescope layout

Figure 2.3: MST Schwarzschild-Couder design segmentations for CTA. Left: the Primary mirror segmentation in 16 elements P1 of the inner ring and 32 mirrors P2 of the outer. Right: the segmentation of the secondary mirror into 8 elements of the inner and 16 of the outer ring (Image from Rousselle et al. 2015).

2.3 Mirror description

Schwarzschild was first finding analytical formulas for the figures of the mirrors, based on the requirement of the complete correction of the spherical and comatic aberrations near of the axis of the optical system. His solutions are named after him and are known as Schwarzschild aplanats. The definition of the mirror surface is rotationally symmetric and the height of it as well as its slopes depend on the radius only. There is also an approximating polynomial for each mirror surface. For detailed explanation on both, the secondary and the primary mirror and on their curvature and slopes, have a look at Vassiliev & Rousselle (2012). Based on the fact that in this thesis is only dealt with a P2 mirror segment, the description of the primary mirror is given in the following.

Surface definition

The location of a infinitesimal small surface element can approximately be described in cylindrical coordinates by the given equations below.

$$\frac{1}{F}x\left(\tau,\Phi\right)=\sqrt{\tau}cos\Phi \tag{5}$$

$$\frac{1}{F}y\left(\tau,\Phi\right)=\sqrt{\tau}sin\Phi \tag{6}$$

$$\frac{z\left(\tau\right)}{F}=Z\left(\tau\right) \tag{7}$$

$$\tau=\left(\frac{\mathrm{r}}{F}\right)^{2}=\frac{x\left(\tau,\Phi\right)^{2}}{F^{2}}+\frac{y\left(\tau,\Phi\right)^{2}}{F^{2}} \tag{8}$$

With r, the radial distance to the optical axis of the telescope, $\tau=\frac{r^2}{F^2}$, Φ the azimuth angle and x, y and z, the three Cartesian coordinates of the system. At least Z has an exact analytical definition (equation 9), which can be Taylor expansioned, to an approximative definition (equation 10).

$$Z\left(\tau\right)=\frac{1}{486}\frac{\tau}{\left(1+\sqrt{1-\tau}\right)^{3}}\left(47+141\sqrt{1-\tau}+171\left(1-\tau\right)+73\left(1-\tau\right)^{1.5}\right) \tag{9}$$

$$\begin{aligned}Z\left(t=\tau-\frac{7}{16}\right)=&+1.4237\cdot10^{-6}+0.11107t+6.4869\cdot10^{-3}t^{2}\\&-6.0375\cdot10^{-3}t^{3}+1.4912\cdot10^{-2}t^{4}-5.6809\cdot10^{-2}t^{5}\\&+0.13774t^{6}-0.24615t^{7}+0.30847t^{8}-0.26204t^{9}\\&+0.13550t^{10}-3.3061\cdot10^{-2}t^{11}\end{aligned} \tag{10}$$

3 Phase measuring deflectometry

Phase measuring deflectometry (PMD) is a deflectometric method, developed by the Optical Sensing, Metrology and Inspection (OSMIN) group of prof. G. Häusler at the University of Erlangen–Nürnberg. Phase measuring deflectometry method is for the fast full-field measurement of specular free-form surfaces. In principle, the slopes of the surface had to be measured. Therefore, predefined patterns reflected by the tested surface have to be evaluated, to achieve measurement uncertainties of around 150 arcsec (see Knauer 2006).
The following subsections show how PMD works from Pixel mapping via optimisation of the mirror position to the calculation of the point spread of the mirror. For more information see Knauer (2006) and Häusler (1999).

3.1 Measuring setup

In general, a PMD measuring setup consists of the surface to be tested, a TV screen and several cameras (see figure 3.1). Their number depends on the size of screen and surface. By the knowledge of position and orientation of each, the single images can finally merged to one. The two setups at University Erlangen-Nürnberg, called short-working-distance-2 (SWD-2) and short-working-distance-3 (SWD-3) (shown in the figures 8.1 and 8.2 in the appendix) use four cameras to cover the whole telescope mirror, which is to be tested.

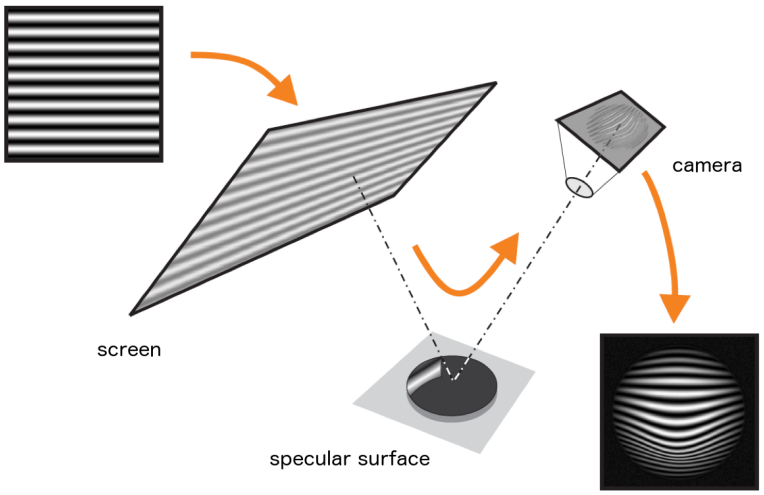

Figure 3.1: Plan of the PMD setup. The camera detects the sinusoidal pattern reflected by the specular surface and projected by the screen (Image from Knauer 2006).

3.2 Pixel mapping

In case of knowing the spatial coordinates of every single pixel of the screen respectively of the projected patterns and of the camera chip, by knowing rotation and position of each setup part, slopes can be calculated like shown in figure 3.2.

In reality, setup behaviour is different. While location and orientation of screen and cameras are still known, the location and orientation of the surface to be tested, differ from perfect assumption.
To achieve this information each pixel of the TV screen has to be assigned one to one towards the camera. One of the most obvious ways probably would be to turn on each TV pixel on his own and see in which camera pixel the light is detected. One problem of this method is the inadequate time requirement. Especially nowadays, with increasing number of pixels in screens, also the expenditure of time increases. The smarter way is to use sinusoidal patterns going through the screen by phase shifting. In fact, doing this twice with a small and a large period of sinusoidal patterns, the result is a clear one-dimensional screen to camera pixel mapping. Using the density distribution of the pattern by measuring twice again, horizontally and vertically, the pixel mapping can be obtained much faster.

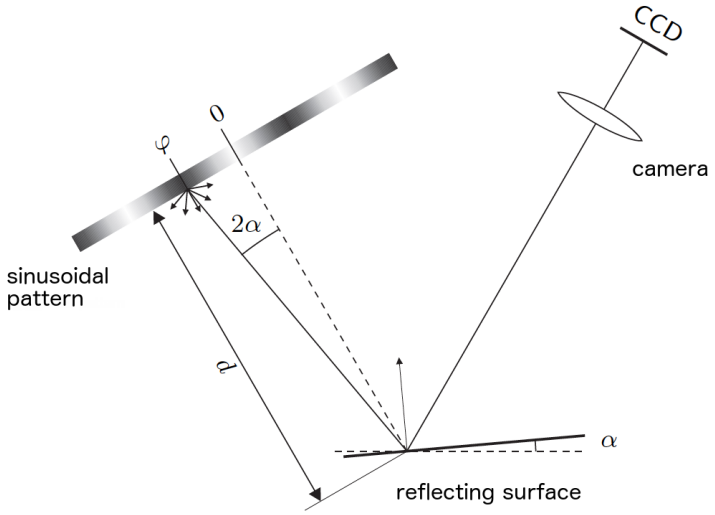

Figure 3.2: The surface normal and slope can be calculated based on the screen to camera pixel mapping. The sine phase ϕ is a measure for the local slope α (Image from Knauer 2006).

3.3 Optimisation of mirror position

In the last step before calculating the spread function, position and rotation of the tested surface have to be determined. Problems appear by ambiguity in the pixel mapping, because of the unknown location, rotation and shape of the mirrors, see figure 3.3.
Surface description of the mirror, by allowing to determine the best–fit location and orientation of the mirror in space, could be an adequate solution. Therefore, a virtual mirror surface model is moved in space until the length between the screen pixels which got hit by the reflected sight rays and the screen pixels that should be hit[4] is minimal. After this optimisation real parameter of location and

[4]determined by the screen pixel to camera pixel mapping

orientation corresponds, expect of mirror uncertainties to them of the best-fit. With this knowledge, it is possible to calculate the slopes like described above.

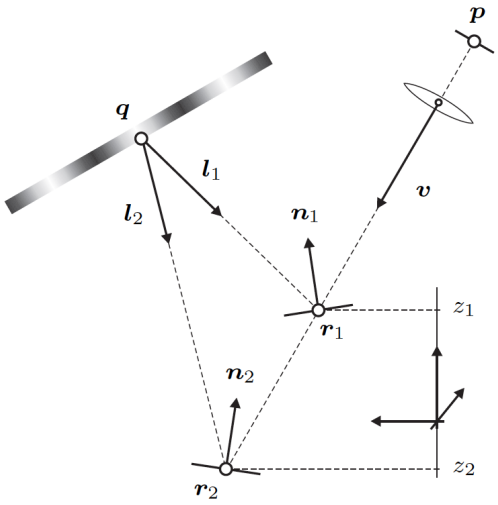

Figure 3.3: Multiple surface slope-height combination leading to an ambiguity at the screen camera pixel mapping (Image from Knauer 2006).

3.4 Point spread function

Defined as the response of an imaging system to a point–like light source, the point spread function (PSF) can be determined by the through PMD calculated slopes of the surface. For spherical mirrors, the response is characterised by the d80 parameter. This is a diameter of a circle where 80% of the point-spread is contained. This gives a possibility of analysation and information about imaging quality of the mirror. The PSF-analysis is a simulation of parallel incoming light waves, represented by lines, which were reflected by the calculated slopes pinned on a simulated perfect mirror surface. After the reflection, the PSF is obtained through capturing the light in the focal plane of the mirror. A result of such an analysis can be seen in figure 3.4.

3.5 Point spread of an aspherical mirror

Aspherical mirrors have an astigmatic form and therefore feature two different curvatures. One corresponds to the radial base vector $\overrightarrow{r}$ which will be called tangential curvature and the other one corresponds to the angular base vector $\overrightarrow{\Phi}$ which will be called sagittal curvature. Both curvatures can not be described by a single radius and accordingly have no clear focal point. Instead, the measured PS contains a focused part and a much larger part, which is out of focus. A single line would be obtained as a PS if it was possible to follow the distribution of curvature radii exactly. Accordingly the d80 parameter used for spherical mirrors is not applicable because it describes a circular containment. Instead, the PS is described as an ellipse with two individual diameters u and v, corresponding to the two radii. This allows to characterise the point spread for sagittal and tangential

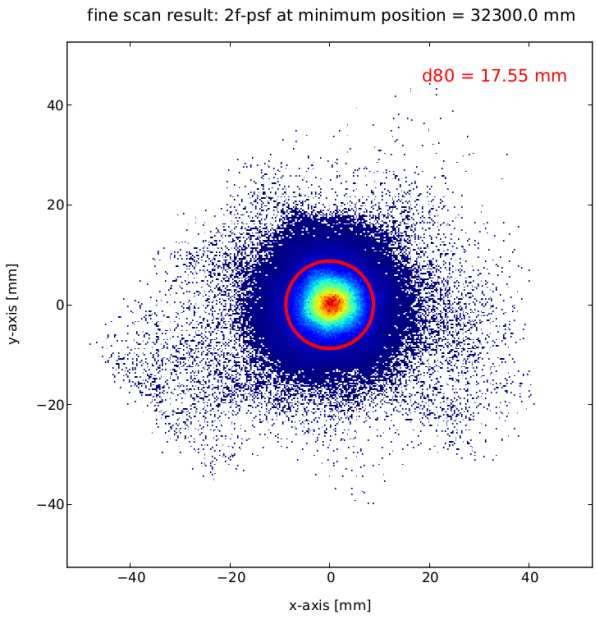

Figure 3.4: Minimal point spread of a spherical telescope mirror with a sphere radius of 32m. The d80, 80% containment circle diameter is 17.55mm and has its minimal position at 32.3m (Image from Specovius 2016).

curvature independently. The diameters u and v are determined as the standard deviation of the point spread in the corresponding axis, see figure 3.5. The PSF for both curvatures is related to the PSs with minimal u and v respectively. The distance to the mirror in which the minimal u and v can be observed corresponds to the most suitable curvature radii or focal lengths, depending on measuring method.

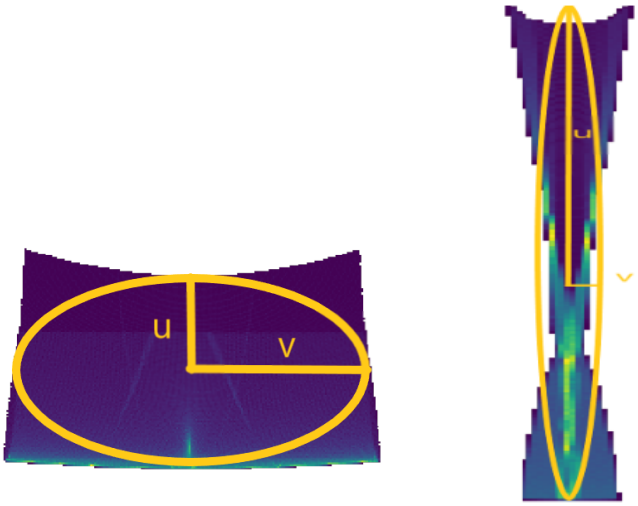

(a) (b)

Figure 3.5: Point spreads with minimal diameters u and v. For illustration, sketches of the describing ellipses are printed over the point spread. It can be seen that the point spread contains focused areas as well as larger ones that are out of focus.

4 Measurement of small size mirror

It has been shown that the developed procedure works quite well for the measurement of spherical telescope mirrors (see Wörnlein 2012). In order to prove this, a spherical sanko mirror with a curvature radius of 32m was available at ECAP. This mirror is used for reference measurement, for the small mirror, as well as for the aspherical mirror P2. Going more in detail, this section is about evaluating a small size mirror (see figure 4.1), with an curvatur radius of $30m$ and a diameter of 20cm, by using the sanko-3 as reference. It is shown which modifications to the default PMD evaluation procedure for spherical mirrors are applied and what results can be achieved.

Image merging

As already mentioned multiple cameras are necessary for telescope mirrors in order to measure the surface completely in a short distance. Because exact camera position and rotation is essential for measurement and eventualities in environmental influences can not be excluded, recalibration of all cameras is applied in every evaluation.
In case of small surfaces and more than one camera in the setup, problems appear through recalibration. Every camera observes a different surface element of the sphere. So each of the cameras is repositioned during the calibration process. As a result, for a small observation surface, the individual images can not be merged adequately to one. This is shown in figure 4.2(a).

Figure 4.1: Above, a small size mirror at Erlangen Centre for Astroparticle Physics with a curvature radius of 30m and a diameter of 20cm

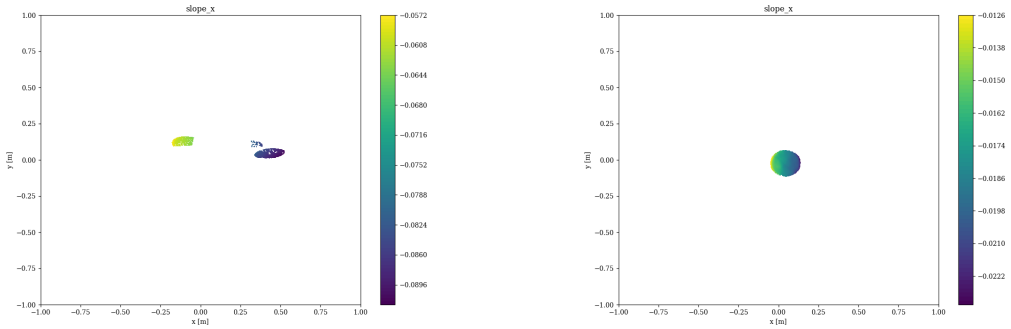

(a) without reference surface

(b) with reference surface

Figure 4.2: Slopes in x-direction are plotted with colors against x and y direction. On the left image merging does not work, so all four images are randomly spread. In plot (b) all four images are merged to one with a high accuracy.

This problem can be solved by measuring the small spherical mirror in combination with a huger reference mirror. The reference is used for recalibrating the setup while the smaller is actually measured. The merged image now has the same quality like the associated one for the reference mirror alone. That this method workes quite well, can be seen in 4.2 (b). By using the shown evaluation technique a PMD evaluation and analysis of the point spread is now possible.

Point spread

In the following, the sperical radius of the previously merged mirror is determined with a ray tracing. Here there are to possible methods to apply. In both ways, light rays propagate onto the mirrors surface model, produced during PMD evaluation. The incoming light is reflected on the surface by using the also through PMD evaluation obtained slopes.
With the first method, the mirror's focal length can be obtained, by using a simulated source, which propagates light rays parallel to the optical axis of the mirror. Named is this method 1f, coming from the result of the measurment, the focal length. Second measuring opportunity, the 2f measurement, serves the curvature radius, by sending out light from a point source, located on the optical axis. The reflected light is then analyzed at the point of emission.
To obtain the focal length and the curvature radius the PSs of the reflected light are scanned for the minimal d80 value. In figure 4.3 the dependency of the d80 value from the distance to the mirror surface on the optical axis is shown for the in this section with PMD evaluated mirror.

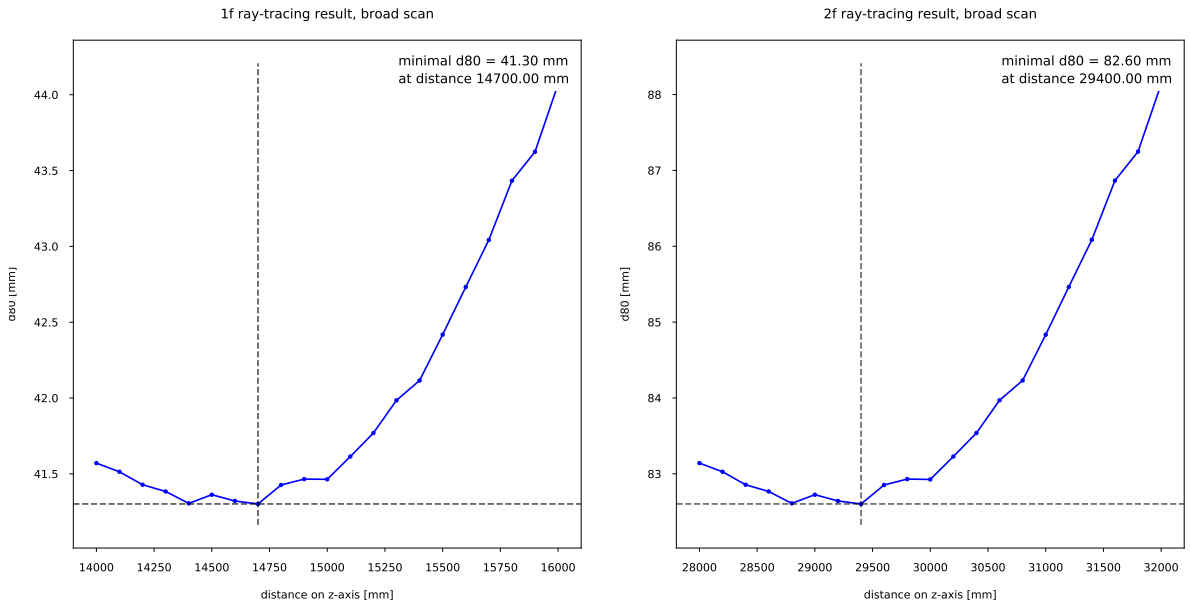

Figure 4.3: Minimization d80 results for the 1f (left) and the 2f (right) methode. In both cases a minimum is found at a value near the ideal values for focal length and curvature radius (see table 4.1)

A minimum for the d80 value was found and is listed with the obtained curvature

radius and focal length, in table 4.1. Figure 4.4 shows the minimal d80 circle at the calculated distances for 1f and 2f measurement.

	2f: curvatur radius	2f: d80	1f: focal length	1f: d80
ideal mirror	30m	(point)	15m	(point)
measurement	29.4m(-2%)	82.6mm	14.7m(-2%)	41.3mm

Table 4.1: Curvature radii, focal lengths and point spreads of the small size mirror for minimal d80 value.

In table 4.1 it can be seen, that there is only a deviation of 2% in the curvature radius measured with the 2f method to the ideal value. For the measurement of the focal length there is also a deviation of 2% compared to the ideal value. Interesting are the, large d80 values of 41.3mm (1f) and 82.6mm (2f), compared to the evaluation of the sanko mirror in chapter 6.1 (d80(1f)=8.31mm, d80(2f)=16.61mm). Summed up, on the one hand, measuring and evaluation of small mirrors are possible and can be done with adequate method. On the other hand, the accuracy of the curvature radius, the focal length and the point spread becomes worse by measuring smaller mirrors.

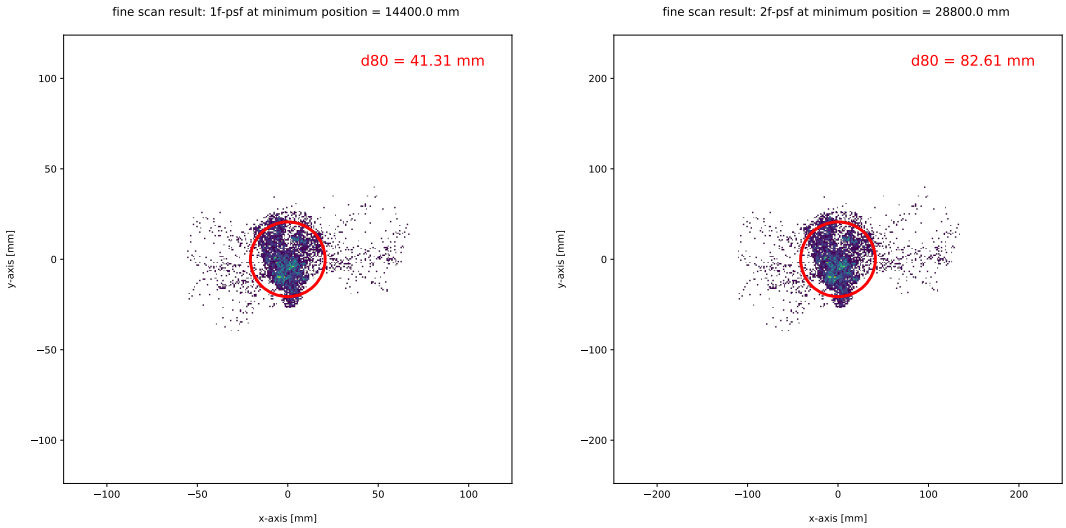

Figure 4.4: Ray tracing of a small spherical mirror with curvature radius of 30m. The focal plane can be resolved during ray tracing. On the left the result for 1f and the right that of the 2f methode. The d80 value of f1 is, as expected, roughly double of the 2f measurement.

5 Measuring aspherical mirror P2 facets

In this chapter a simulated aspherical P2 mirror will be measured and evaluated, to get information about systematics involved in the evaluation process. For this, the differences of evaluation to standard spherical mirror evaluation will be described. In the second part of this chapter a real aspherical mirror is evaluated in the same way as the simulated, to compare the results of both.
As explained and already used in chapter 3.3 and 4 a surface model is needed for the evaluation to avoid ambiguity in PMD measurement. Specovius (2016) has shown, that it is handy to use a rotationally symmetric prolate ellipsoid (ilustrated in figure 5.1) to describe the aspherical mirror, with its two individual curvatures, as the underlying surface model for evaluating a P1 mirror. Based on this both, the ideal and the real P2.029 mirror, were tested to learn whether this approach for even more curved mirrors works, as well.

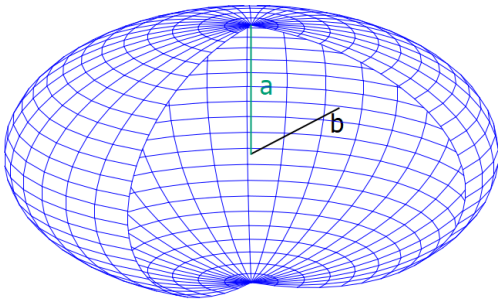

Figure 5.1: Model of a rotationally symmetric prolate ellipsoid. It is rotational symetric along the c radius.

5.1 Measuring simulated aspherical mirror

The simulations of spherical telescope mirrors have been developed by Pickel (2014) and were integrated in the program Mitsuba, to do PMD evaluation. Afterwards Specovius (2016) used this simulation to work on aspherical mirrors, by approximating them by a finite number of triangles. So it was also done for the P2 mirror. The so obtained surface description was integrated in the simulation program Mitsuba to evaluate the aspherical mirror facet. The PMD evaluation of this simulated mirror, with its known sagittal and tangential curvature radii gives information about the systematics in measurement and evaluation.

Image merging

Common for measuring telescope mirrors there is more than one camera in the test setup. As already discussed in detail in chaper 4, it is handy to use a reference mirror, to improve merging quality. In these theses aspherical mirror image merging is supplied by a spherical reference mirror used for recalibrating the cameras.
Figure 5.2 shows both the results of PMD slope evaluation for the simulated asphere (left) and its also simulated spherical reference mirror (right). The merged

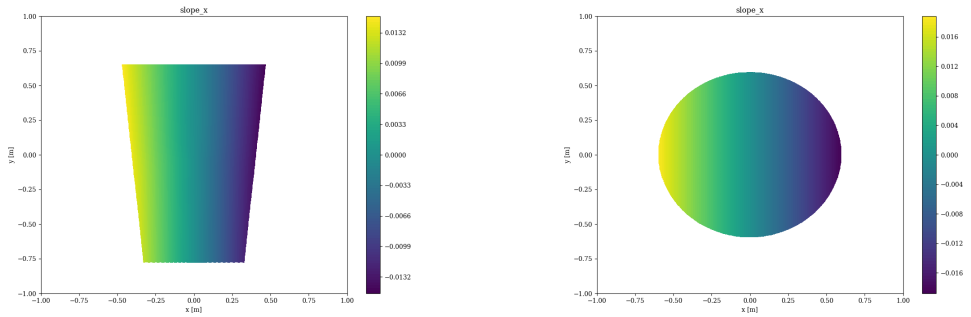

(a) simulated aspherical mirror

(b) simulated spherical reference

Figure 5.2: Slopes in x-direction trough PMD evaluation. On the right the slopes of the spherical reference and on the left the slopes of the aspherical mirror with reference are shown

aspherical surface image now[5] has the same quality like the image of the simulated spherical mirror on his own.

Curvature radii and Point spread

By using the evaluation technique described above, ray tracing and a distinction of both focal planes is possible. Expected for ray tracing is, instead of a circle with the d80 parameter, an ellipse with parameters u and v. Also two focal planes are expected for which the parameters u and v are minimal, depending on the distance. In figure 5.3 the dependency of the distance for u and v is shown and an unambiguous minimum for both parameters is visible. The point spread (seen in figure 5.4), follows also the expected behaviour described in chapter 3.5

curv. radius	model	simulation & evaluation
sagittal	29.58m	29.55(-0.1%)
tangential	47.66m	46.62(-2%)

Table 5.1: Curvature radii from the simulated aspherical P2 mirror compared to the ideal mirror curvature radii of the model, obtained through simulation are listed.

Results of the evaluation are listed in table 5.1. Remarkable is the concordance of the measured and the ideal sagittal curvature radius, determined via tracing the normals of the mathematical surface description, with a mismatch of 0.1%. Not only the deviation between the sagittals is low, but also that of the tangential curvature radii matches within an error of 2%. The minimal u and v spread as another parameter for measurement quality for the 2f ray tracing are shown in table 5.2. As expected the minimal u spread is much lower than the minimal spread of v. Responsible for this, is the strongly increasing curvature in this direction of the mirror. In sum there are less systematics in evaluation measurable.

[5] without reference merging is faulty

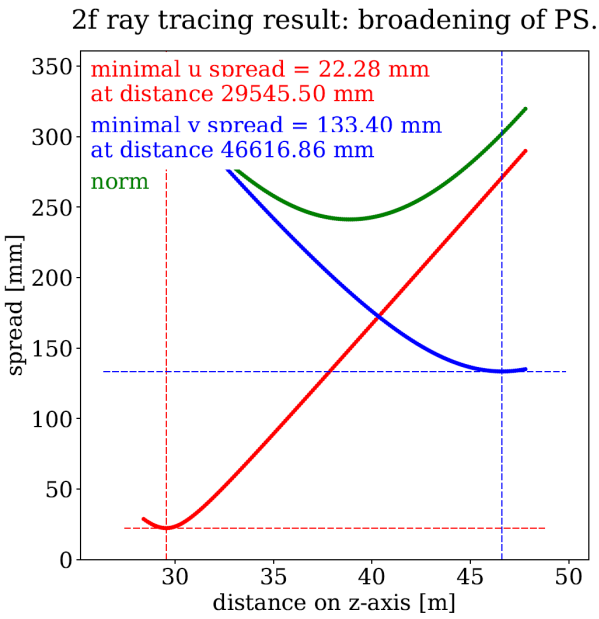

Figure 5.3: Simulated aspherical mirror: Dependency of the spread parameters u and v on the distance to the mirror. Both curvature radii can clearly be resolved from just one measurement. The best–fit ellipsoidal radii are 29.55m and 46.62 m.

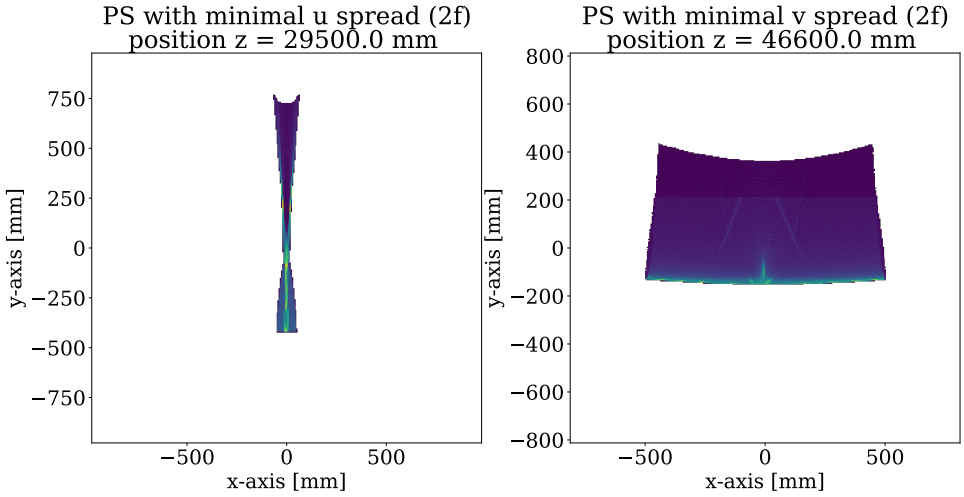

Figure 5.4: PSs of the simulated aspherical mirror from scan planes close to the positions with the minimal spread parameters u and v (minima in fig. 5.3).

minimal spread	model	simulation & evaluation
u	x like shape	22.28mm
v	x like shape	133.4mm

Table 5.2: The minimal u and v spread for the 2f ray tracing from the simulated aspherical P2 mirror

5.2 Measuring real aspherical P2.029 mirror

Previously PMD measurement was implemented for simulated ideal aspherical mirrors, with a simulation of a P2 mirror. In the next step, evaluation is applied to a real version of this mirror P2.029, which is produced for a prototype medium size Schwarzschild-Couder telescope (see figure 5.5). P2 Mirror has a size of about 1.45m from the bottom to the top and about 0.95m between the flanks and so covers a segment area of $1.16m^2$. Compared to a P1 mirror, the P2 of the outer primary ring is 40cm less wide but about 20 cm higher.

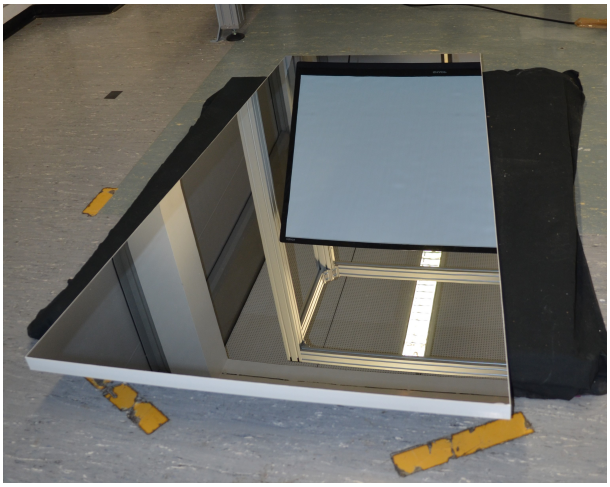

Figure 5.5: A fore medium size Schwarzschild-Couder telescope produced P2 mirror segment available at Erlangen Centre for Astroparticle Physics. Product description: P2.029.

Curvature radii and point spread

Curvature radii and point spread are obtained in the same way, like for the simulated mirror before. Figure 5.7 shows the dependency of the spreads u and v on the distance to the mirror and figure 5.6 shows the corresponding PSs with the minimal spreads u and v. The PSFs for tangential and sagittal curvature are reproduced astonishingly well.
Results of the evaluation are listed in table 5.3. Remarkable is the concordance of the measured sagittal curvature radius of the simulated and the real P2 mirror, with a mismatch of 0.14%. Not only the deviation between the sagittals is low, but also that of the tangential curvature radii matches within an error of 2.17%. The minimal spread u and v spread as another parameter for measurement quality for the 2f ray tracing are shown in table 5.5.

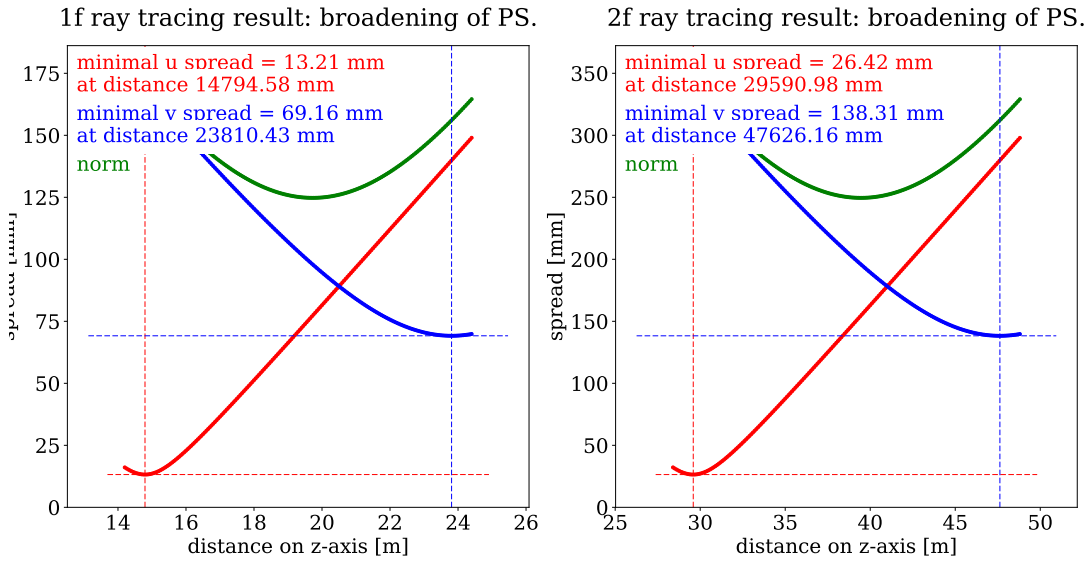

Figure 5.6: Measured P2: Dependency of the spread parameters u and v on the distance to the mirror. Again both curvature radii can clearly be resolved from just one measurement. The best–fit ellipsoidal radii were 29.6m and 47.63 m.

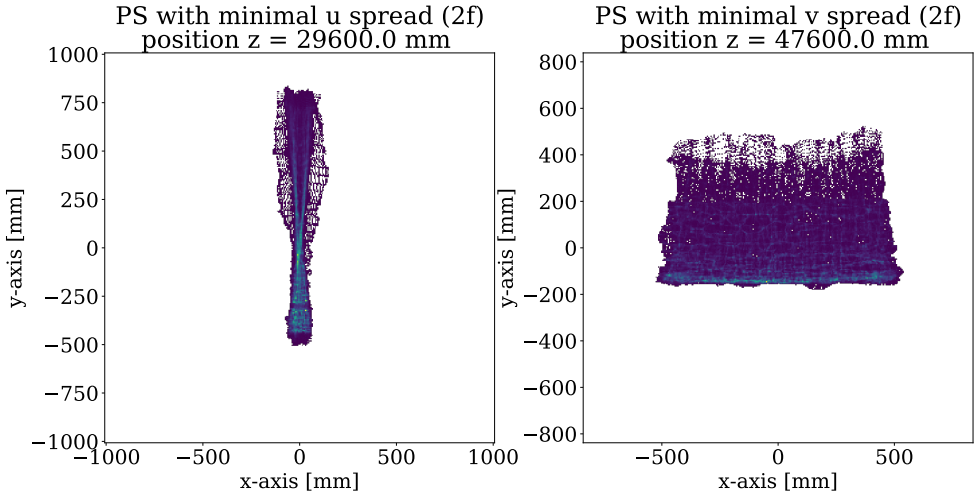

Figure 5.7: PSs of the aspherical mirror P2 from scan planes close to the positions with the minimal spread parameters u and v (minima in fig. 5.6).

curv. radius	simulation & evaluation	real mirror
sagittal	29.55m	29.59m(+0.14%)
tangential	46.62m	47.63m(+2.17%)

Table 5.3: Curvature radii from the aspherical P2.029 mirror compared to those of the simulated and evaluated mirror.

5.3 Comparison and discussion

Within the two PMD evaluations and ray tracings, of the simulated and real P2 mirror, a comparison is possible. In table 5.4 the tangential and sagittal curvature radii obtained through evaluation are listed. The determination of the curvature radii has worked pretty well in both cases. As expected, because of elimination of systematics in the direct comparison of model and real mirror, the deviations of the P2.029 mirror to the ideal mirror[6] are smaller than those of the simulated mirror to the ideal one.

curv. radius	model	simulated & evaluated mirror	real mirror
sagittal	29.58m	29.55(+0.10%)	**29.59m**(-0.03%)
tangential	47.66m	46.62(+2.18%)	**47.63m**(+0.06%)

Table 5.4: Curvature radii from the simulated aspherical P2 mirror compared to those of the real P2 mirror and the ideal mirror curvature radii, obtained through simulation.

Furthermore another criterium for comparing, the minimum spread, can be looked at. The minimal u and v spreads shown in table 5.5 are worse for the real mirror, compared to the simulated one. The deviation is 3.68% for the minimal u spread and over 18% for the minimal v spread.

minimal spread	simulated & evaluated mirror	real mirror
u	22.28mm	26.42mm(+18.58%)
v	133.4mm	138.31mm (+3.68%)

Table 5.5: The minimal spread parameters u and v for the 2f ray tracing from the simulated aspherical P2 mirror compared to those of the real P2.029 mirror

[6]The calculated deviations of the simulated and evaluated mirror to the ideal mirror are the systematics of the evaluation

6 Comparison of SWD-2 and SWD-3

In this part of the evaluation, the previously for reference measurement used spherical sanko mirror will again be evaluated in the already known way (see chapter 3 Measuring with SWD-2 setup). Further more PMD evaluation will be done with the swd-3 measuring setup to compare the two setups. Pictures and a short introduction on the setups can be found in figure 8.1 for SWD-2 and in figure 8.2 for SWD-3 in the appendix.

6.1 Measurement of sanko mirror with SWD-2

In this evaluation no reverence mirror is needed. In figure 6.1 the slope deviation in x direction of the surface slope compared to an ideal sphere, is shown. As it can be seen, there are no distortions on the edges and in the surface. Consequently improving image merging through recalibration of the cameras during measurement worked well. The white asymmetric triangle, which could be seen in figure 6.1 is a white paper (see figure 8.1), with the same shape, which is fixed on the mirror to clarify mirror orientation in measurement and at the setup. After the

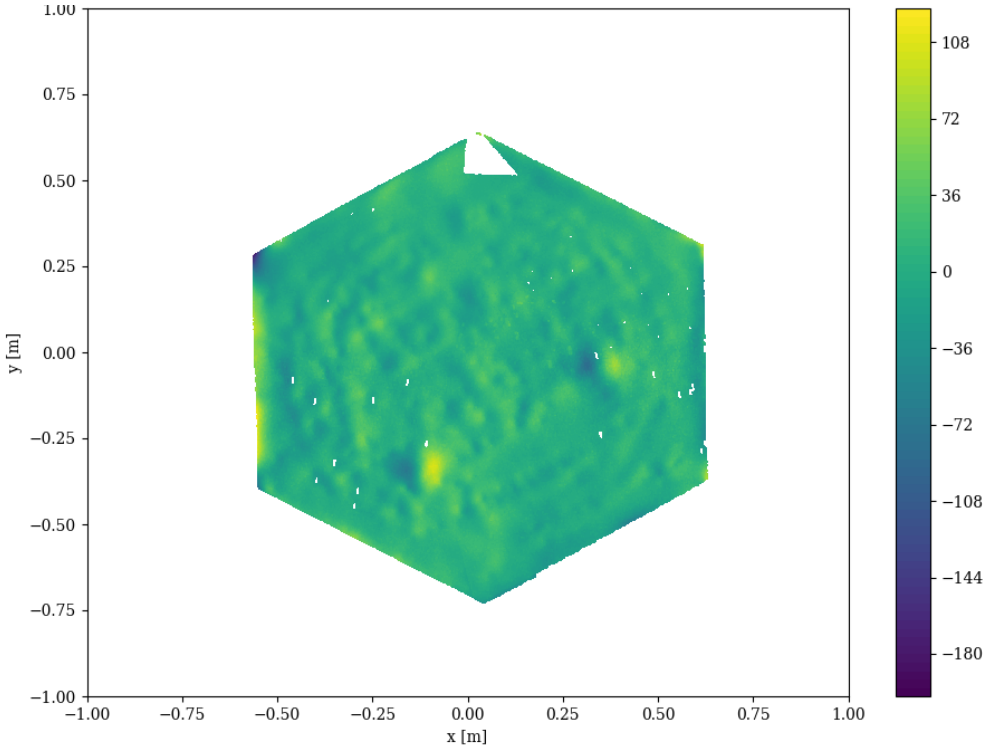

Figure 6.1: Slope deviation in x-direction trough PMD evaluation, using the SWD-2 measuring setup. The white asymmetrical marker is used for getting orientational informations in of the setup and do not hinder evaluation. The white corner can also be seen in the picture to compare orientation in setup and in evaluation. The two huge deviations came from the suspension of the mirror for the telescope.

pixel mapping, the optimisation of the position of the mirror model and the so

calculated slopes, the position with the minimal point spread was calculated (see figure 6.2). A minimal d80 value could be unambiguously identified for 1f as well as for the 2f measurement technique and is shown in figure 6.3. It will be noted that the point spread subjects to a nicely symetric shape. All results are listed in table 6.1.

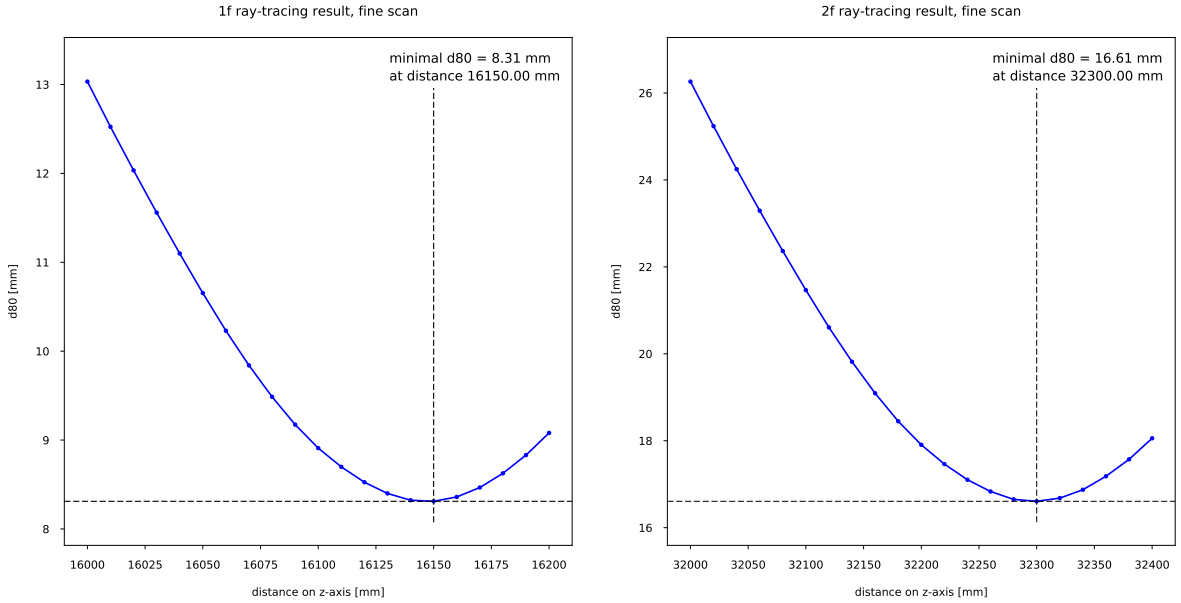

Figure 6.2: Minimization d80 results for the 1f (left) and the 2f (right) method. Evaluation is done with SWD-2. In both cases a minimum is found at a value near the ideal values for focal length and curvature radius (see table 6.1)

	1f: focal length	1f: d80	2f: curvatur radius	2f: d80
ideal mirror	16m	0mm	32m	0mm
swd-2 measurement	16.15m	8.31mm	32.30m	16.61mm

Table 6.1: Point spread of the sanko mirror for minimal d80 value, mesured with the SWD-2 setup.

6.2 Measurement of sanko mirror with SWD-3

Again no reference mirror is needed, because of its spherical shape. The surfaces slope deviation in x-direction is displayed in figure 6.4. It stands out, that the merging with SWD-3 is worse than by using SWD-2, because of the amount of distortions. This was expected, due to previous measurements with the SWD-3 setup. The white asymmetric triangle in the plot is a paper which was fixed at the mirror to get information about orientation in the measurement process. How the paper is fixed at the mirror and how it is located in the SWD-3 setup, can be seen in picture 8.2. Regardless of this, the minimal d80 value of the point spread for the 1f and 2f method could be calculated at a distance of 16.2m for 1f and 32.4m

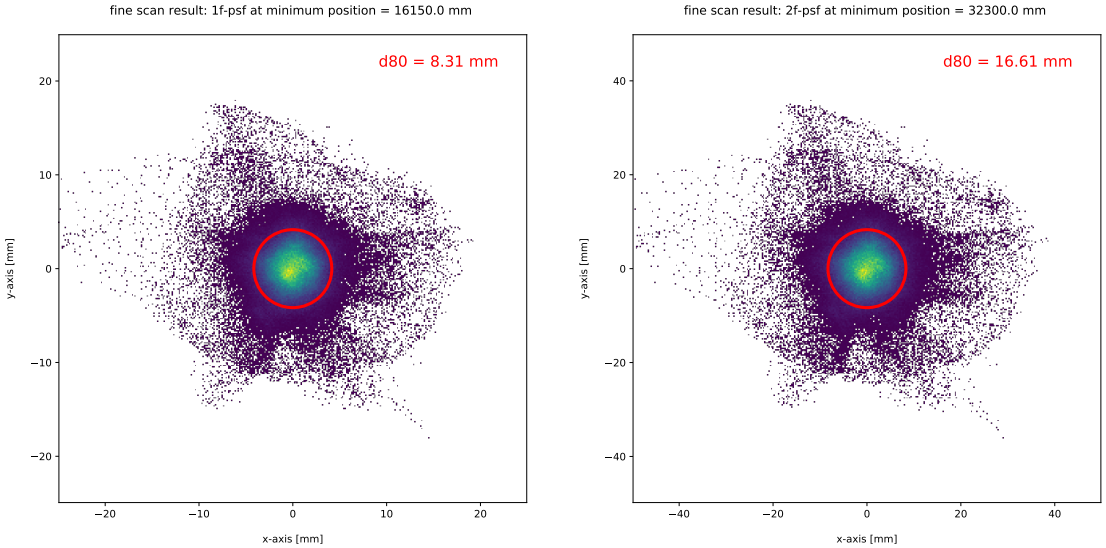

Figure 6.3: Nicely symetric PSs of the spherical mirror P2 from scan planes close to the positions with the minimal d80 value (minima in fig. 6.2). Evaluation is done with SWD-2.

for the 2f measurement (see figure 6.5). The minimal point spread and its d80 value are displayed in figure 6.6, were an other effect, an obviously asymmetric PS, caused by worse merging can be seen. To get an overview of the measurement of sanko mirror with the SWD-3 setup, all results are listed in table 6.2.

	1f: focal length	1f: d80	2f: curvatur radius	2f: d80
ideal mirror	16m	0mm	32	0mm
swd-3 measurement	16.22m	10.30mm	32.44m	20.57mm

Table 6.2: Focal lengths, point spread and curvature radii of the sanko mirror for minimal d80 value, measured with the SWD-2 and SWD-3 setup compared to the values the mirror is made with.

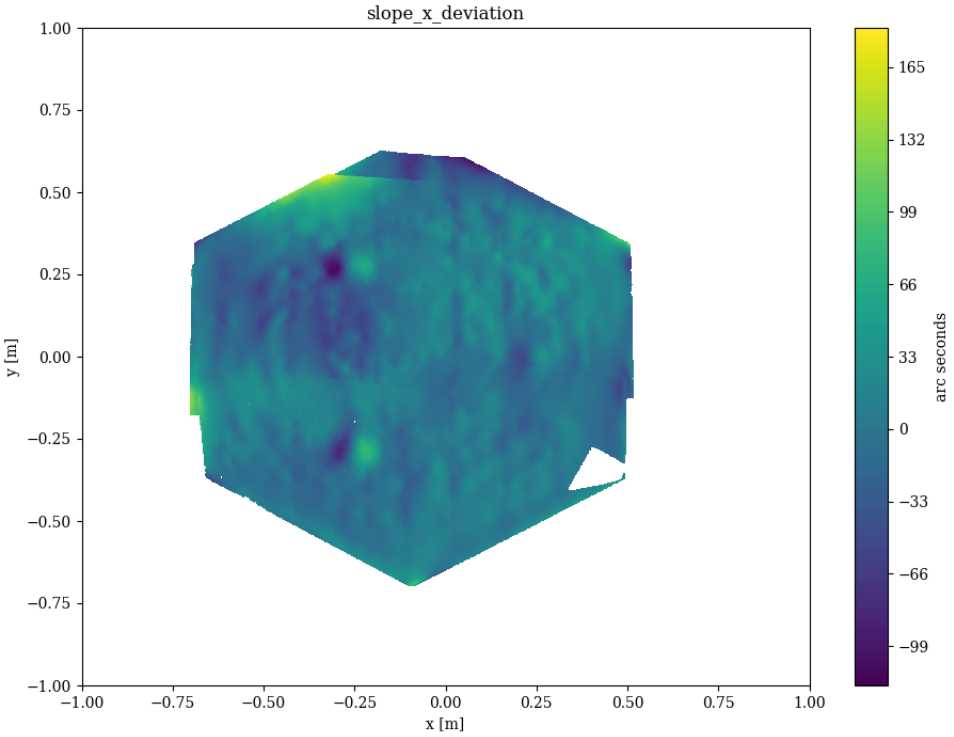

Figure 6.4: Slope deviation in x-direction obtained through PMD evaluation, using the swd-3 measuring setup. The white asymmetrical marker is used for getting orientational informations in the setup and do not hinder evaluation. The white corner can also be seen in the picture to compare orientation in setup and in evaluation. The two huge deviations came from the suspension of the mirror for the telescope.

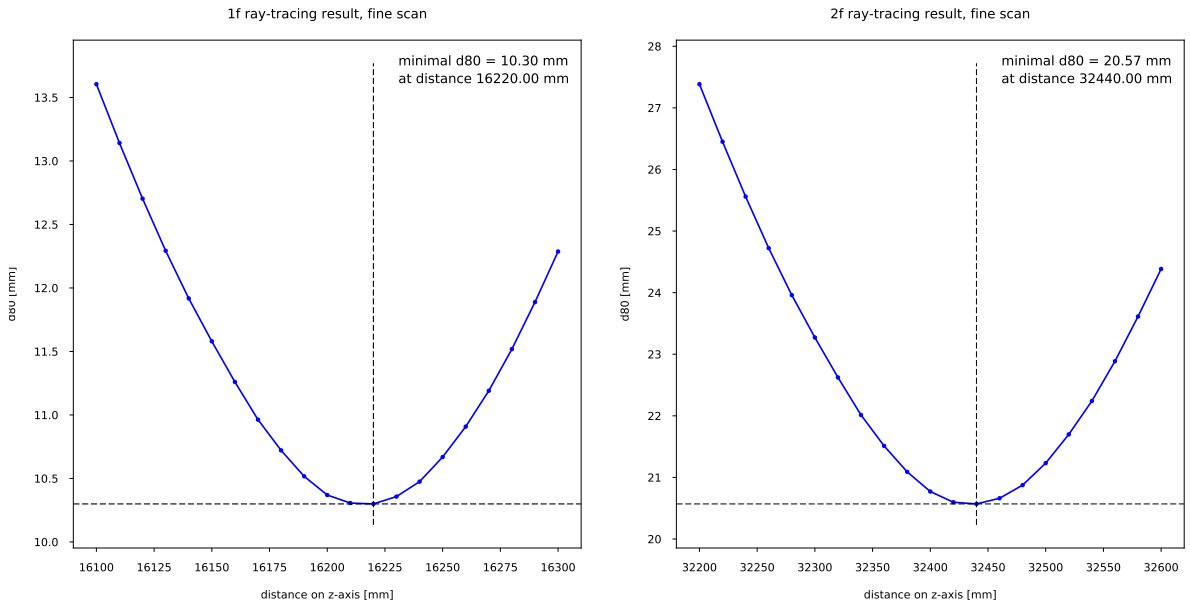

Figure 6.5: Minimization d80 results for the 1f (left) and the 2f (right) method. In both cases a minimum is found at a value near the ideal values for focal length and curvature radius (see table 6.2)

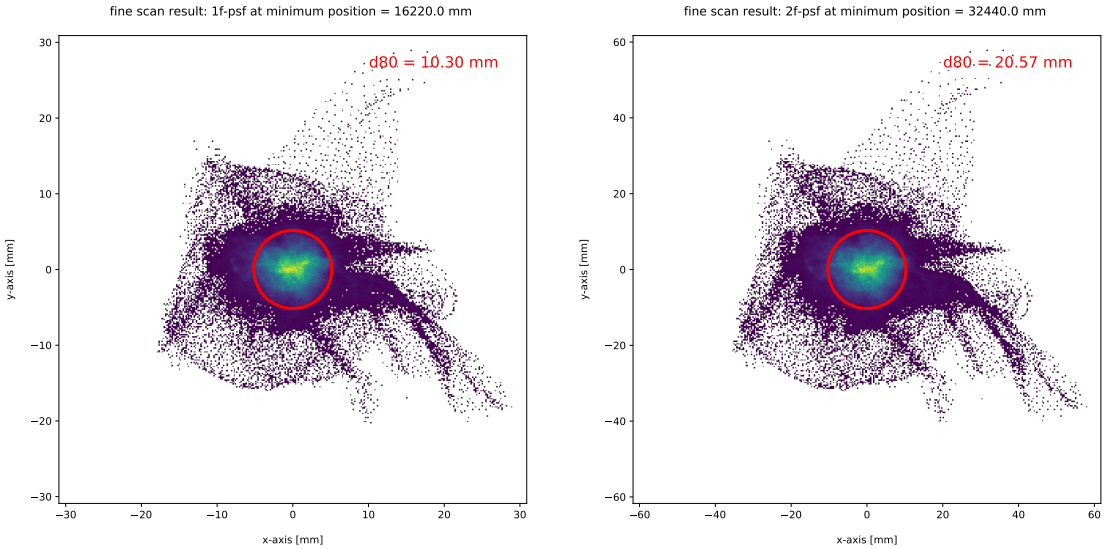

Figure 6.6: PSs of the spherical mirror P2 from scan planes close to the positions with the minimal d80 value (minima in fig. 6.5). The obvious asymmetric effects are caused by merging deficits.

6.3 Comparison and discussion

Within the two PMD evaluations and ray tracings of the sanko mirror, using the two SWD setups, a comparison of both is possible. As already discussed in the previous two subchapters, image merging with SWD-2 works much better than with SWD-3 (keep in mind figures 6.1 and 6.4). Nonetheless evaluations could be made for both in the same way. To compare the measuring accuracy, results for both evaluations listed in table 6.3. Remarkable is on the one hand the

	1f: focal length	1f: d80	2f: curvatur radius	2f: d80
ideal mirror	16m	0mm	32m	0mm
SWD-2 measured	16.15m(+0.94%)	8.31mm	32.30m(+0.94%)	16.61mm
SWD-3 measured	16.22m(+1.38%)	10.30mm	32.44m(+1.38%)	20.57mm

Table 6.3: Focal lengths, point spread and curvature radii of the sanko mirror for minimal d80 value, mesured with SWD-2 and SWD-3 setup, to compare each other. The percentages are the deviation from the ideal mirror focal length and curvature radius.

19.3% smaller d80 parameter of the SWD-2 measurement compared to the SWD-3 measurement for both, the 1f and 2f method. On the other hand evaluation with the SWD-2 setup, originate a focal length of 16.15m with a deviation of 0.94% of the ideal value (16m), while through evaluation with the SWD-3 setup a value of 16.22m and a deviation of 1.38% was obtained. Same deviations were calculated for the 2f, curvature radius measurement.
Summarised evaluation with both setups originate good measurement accuracies with low deviations for focal length and curvature radius. Unfortunately the newer SWD-3 setup still works worse than the older SWD-2. Responsible therefore could be tensions in the metal construction or problems in calibration of the cameras with the dot pattern, which is utilised. In the future a new metal made calibration pattern is planned to be used to avoid uncertainties through calibration.

7 Summary and outlook

Goals of this thesis are to measure asperical P2 mirror for the Schwarzschild-Couder telescope for the fist time and show improvements in measurements of small size mirror. Furthermore a comparison of two measurement setups, both located at University-Erlangen-Nürnberg was done. This includes modifications done by Specovius (2016), to allow aspherical mirror evaluation. Due to this fact the measuring technique phase measuring deflectometry (Wörnlein 2012), which is well established for measuring CTAs spherical telescope mirrors, is described. Before this, two designs for medium size telescopes for CTA were introduced. More in detail on the Schwarzschild–Couder layout, a mathematical surface definition and segmentation of the mirrors of the primary dish was given. With this information, phase measuring deflectometry was introduced for spherical and aspherical mirror surfaces. First measured and evaluated mirror was a small mirror with a diameter of 20cm. Problems of calibration were announced and solved. Second measurement was about a aspherical mirror of the Schwarzschild-Couder telescope. Therefore an evaluation of a simulated facet was compared to one of a real P2.029 mirror. At least a comparison on the two short working distance measuring setups located at university Erlangen-Nürnberg was done, to have a lock at sensitivity and quality of the newer SWD-3 setup in its current status.
One of the results of this thesis indicates that the new ellipsoidal evaluation approach also seems to be promising for measuring the P2 type SCT mirror facet. Nevertheless, also the ellipsoidal surface model constitutes only an approximation of the exact surface structure of the aspherical mirror facets so more studies on aspherical mirrors have to be done.
Another result is that PMD evaluation also works pretty well for small size spherical surfaces by using a larger reference surface for calibration. After all the measuring setup comparison brought some results. The newer SWD-3 setup works better than before calibration, but still not as good as the older SWD-2. Reasons could be tensions in the metal construction or problems in camera calibration with the dot pattern being in use. Aims for the future should be improving calibration techniques for SWD-3 to obtain a better accuracy in PMD measurement. Furthermore construction should be controlled for tensions.
At the end it is important to keep in mind that measuring the quality of single spherical and aspherical mirrors is a step that is necessary in order to analyse the imaging quality of SCTs. The aim is to measure the amount of light that finally finishes up in one pixel of the telescope camera. This information can hardly be obtained by measuring just one single mirror facet.
The results of these studies will help to improve measurement with the two SWD setups of aspherical mirror facets of CTAs medium sized SCTs.

8 Appendix

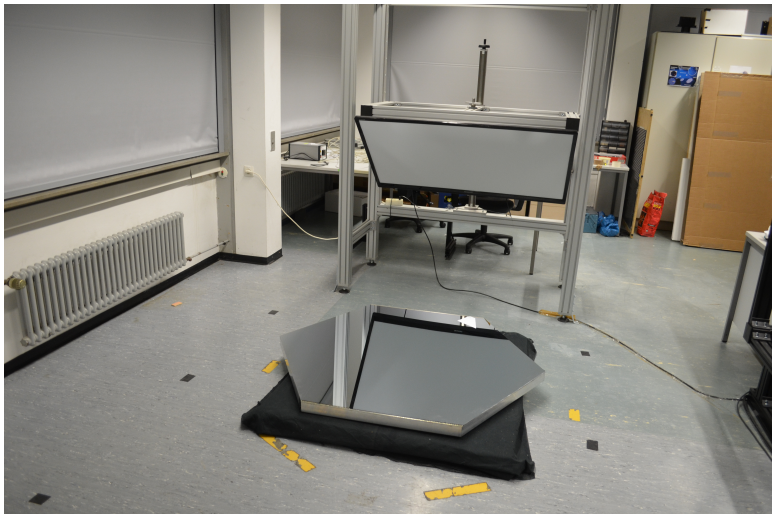

Figure 8.1: Short-working-distance-2 measuring setup with TV-screen and the sanko mirror. The four cameras focused on the mirror, are located in the back. The white asymmetric paper fixed on one edge of the mirror is for orientation.

Figure 8.2: Short-working-distance-3 measuring setup with a TV-screen on the left, a standing fixed sanko mirror in the middle and the 4 cameras on the right sight of the picture. The white asymmetric paper fixed on one edge of the mirror is again for orientation and comparison of the mirror location in the two measuring setups.

References

Acharya, B. S., Agudo, I., Samarai, I. A., et al. 2018, Science with the Cherenkov Telescope Array

Balzer, A. 2012, The H.E.S.S. Data Acquisition System an overview, https://www-zeuthen.desy.de/technisches_seminar/texte/Balzer_Zeuthen_20120626.pdf

Blasi, P. 2009, Physical Review Letters, 103, 051104

Blümer, J., Engel, R., & Hörandel, J. R. 2009, Progress in Particle and Nuclear Physics, 63, 293

Consortium, C. 2018, Official website of CTA, https://portal.cta-observatory.org/Pages/Preparatory-Phase.aspx

CTA-Colaboration. 2017, MST - Cherenkov Telescope Array, https://www.cta-observatory.org/project/technology/mst/

CTA-Colaboration. 2018, SCT - Cherenkov Telescope Array, https://www.cta-observatory.org/project/technology/sct/

Cui, W. 2009, TeV Gamma Ray Astronomy, Research in Astronomy and Astrophysics 9 (2009) 841-860

Durham University. 2014, Ground Based Gamma Ray Astronomy, https://www.dur.ac.uk/cfai/vhegammaraygroup/physics/groundbased/

Häusler, G. 1999, Method and apparatus for determination of the shape or of the imaging properties of reflective or transparent objects, dE Patent App. DE1,999,144,354

Knauer, M. 2006, PhD thesis, Friedrich-Alexander-Universität Erlangen-Nürnberg

Longair, M. S. 1992, High Energy Astrophysics: Volume 1, Particles, Photons and Their Detection - (Cambridge: Cambridge University Press)

Pickel, S. 2014, Master's thesis, Friedrich-Alexander-Universität Erlangen-Nürnberg

Rousselle, J., Byrum, K., Cameron, R., et al. 2015, Construction of a Schwarzschild-Couder telescope as a candidate for the Cherenkov Telescope Array: status of the optical system

Specovius, A. 2016, Master's thesis, Friedrich-Alexander-Universität Erlangen-Nürnberg

Stanford University, H. A. 2014, An Introduction to Cherenkov Radiation, https://www.dur.ac.uk/cfai/vhegammaraygroup/physics/groundbased/

Tinivella, M. 2016, A review of Cosmic-ray electrons and fermi-LAT

Vassiliev, V. V. & Rousselle, J. P. 2012, Optical System of 9.5m Schwarzschild-Couder Telescope for CTA

Vassiliev, V. V. & Rousselle, J. P. 2013, Segmentation schemes for primary and secondary mirrors of the Schwarzschild-Couder telescope for CTA

Wörnlein, A. 2012, Methods to measure optical properties of mirror facets for CTA

Acknowledgements

I would like to thank everyone who has supported me during my bachelor thesis. Special thanks to:

- Prof. Dr. Christopher van Eldik for giving me the opportunity to work on this interesting subject and for supervising my thesis.
- Andreas Specovius for the great support and for his valuable comments.
- Benjamin Schwab and Sebastian Konrad for making our office a place where effective work as well as enjoyable free time were possible.
- The whole CTA and H.E.S.S group for providing a pleasant working atmosphere.
- My friends for their help, having an open ear and their helpful comments.
- My parents and grandparents for supporting me during my thesis and for enabling my whole studies.

Statement of Authorship

I hereby certify that this thesis has been composed by me and is based on my own work, unless stated otherwise. No other person's work has been used without due acknowledgement in this thesis. All references and verbatim extracts have been quoted, and all sources of information, including graphs and data sets, have been specifically acknowledged.

place, date	signature